International Journal of Heat and Mass Transfer 52 (2009) 5102–5112

Contents lists available at ScienceDirect

International Journal of Heat and Mass Transfer

journal homepage: www.elsevier.com/locate/ijhmt

Bubble growth characterization during fast boiling in an enclosed geometry

S. Escobar-Vargas [a,*], D. Fabris [a,1], J.E. Gonzalez [a,2], R. Sharma [b,3], C. Bash [b,4], O.E. Ruiz [c,5]

[a] *Mechanical Engineering, Santa Clara University, 500 El Camino real, Santa Clara, CA 95053, United States*
[b] *Hewlett Packard, 1501 Page Mill Road, Palo Alto, CA 94304, United States*
[c] *Department of Mechanical Engineering, University of Puerto Rico-Mayagüez Campus, Mayagüez, PR 00680, Puerto Rico*

ARTICLE INFO

Article history:
Received 10 April 2008
Received in revised form 21 October 2008
Available online 15 June 2009

Keywords:
Bubblea area
Microboiling
Bubble growth
Nonspherical bubble
Homogeneous boiling
Bubble efficiency

ABSTRACT

Microboiling is commonly used in thermal inkjet atomizers (TIJ) and microelectromechanical (MEM) devices. The TIJ and MEM devices performance is closely related to the dynamics of the bubble used to operate them; therefore, it is important to determine the conditions of input energy and power leading to specific bubble dynamics. The objective in this work is the characterization, in a confined space, of the bubble dynamics on a range of input conditions of energy and power and what is the effect of the input conditions on the bubble extractable mechanical efficiency. Mechanical efficiency is defined by the ratio of the integral of the mechanical work (work done by the bubble expansion due to the elevated internal pressure relative to atmospheric pressure minus the increase in bubble surface energy) to the total energy input to the microheater. Bubbles are generated with energies of 7–17 μJ under high heating rates and short pulses in deionized water. Resulting nucleation temperature measurements are consistent with homogeneous nucleation. The bubble lifecycle shows strong dependence on the input heater energy and input heating rate. This work presents new results in bubble growth where growth–shrink–growth derived from specific energy conditions. The bubble growth–shrink–growth may be due to subcooled fluid, local variation in the pressure field, and by the surface tension driven change in curvature of the bubble. Mechanical bubble efficiencies result in small values suggesting most of the energy applied to the heater is distributed in other processes which may include increasing the internal energy of the heater film and the fluid.

1. Introduction

Fast boiling, nucleation times on the order of 10^0 μs and bubble lifetime on the order of 10^1 μs, in enclosed microheaters has been widely used in thermal inkjet atomizers (TIJ) and micro-electro-mechanical systems (MEMS), mechanical actuators, nozzle-diffuser pumps, and mixers [1]. The range of drop and spray application includes the printing of ink; delivering of small and precise amount of fluid for chromatography, precise drug delivery; manufacturing of solar cells, coatings, fabrication of lenses; wiring of conductive circuits; and two phase heat transfer among others [2–8]. The wide range of spray applications leads to large efforts to understand the droplet formation either by mechanic (piezo-electric) or thermal inkjet atomizer (TIJ) and in order to improve droplet formation efficiency.

TIJ delivered droplets are directly influenced by the bubble dynamics; therefore, a controlled bubble evolution is desired to have a better spray quality. Controlling the spray quality and the amount of delivered fluid typically requires generating microscale bubbles with high growth rates.

For microheaters, the reduction in spatial and time scales, surface energy [9,10] and non-equilibrium phenomena [11] drive different dynamics of the bubble nucleation and growth. The boiling process on microheaters at high heating rates depends on the local fluid superheat, availability of nucleation sites (via surface irregularities, thermodynamic fluctuations, and/or the presence of non-condensable gases), and fluid properties [12,13]. Typical bubble nucleation models attempt to predict active nucleation cavity sizes [14], initial radius of vapor embryo [15], and bubble growth in non-uniform temperature fields near heated surfaces [16] for macro-scale systems and under saturated pool boiling regimes. However, in transient microboiling the added factors of heating rate, duration, and spatial localization of the heating source change the nucleation and bubble growth processes.

Substantial experimental work focused on high heating rates and nucleation time measurement has indicated that local fluid

---

* Corresponding author. Tel.: +1 408 554 7896; fax: +1 408 554 5474.
E-mail addresses: sescobarvargas@scu.edu (S. Escobar-Vargas), dfabris@scu.edu (D. Fabris), jgonzalezcruz@scu.edu (J.E. Gonzalez), ratnesh.sharma@hp.com (R. Sharma), cullen.bash@hp.com (C. Bash), oruiz@me.uprm.edu (O.E. Ruiz).
[1] Tel.: +1 408 554 4985.
[2] Tel.: +1 408 554 4459.
[3] Tel.: +1 650 857 3835.
[4] Tel.: +1 650 236 2748.
[5] Tel.: +1 787 832 4040x2548.

0017-9310/$ - see front matter © 2009 Elsevier Ltd. All rights reserved.
doi:10.1016/j.ijheatmasstransfer.2009.05.001

Nomenclature

A	hemispherical cap bubble surface area
E	energy
e	Wheatstone bridge voltage
h	height of hemispherical bubble cap
t	time
P	power
p	pressure
R	resistance
r	radius of curvature
r_1	film radius
T	temperature
V	hemispherical cap bubble volume

Greek symbols

η	efficiency
μ	viscosity
ρ_l	density
σ	surface tension

Subscripts

d	reference point
h	microheater
in	input
l	liquid
m	mechanical
o	ambient
out	output
v	vapor

nears the thermodynamic superheat limit based on the spinodal limit. The high superheat result is supported by multiple direct experimental measurements [11,17–19] and by energy dissipation measurements and heat conduction calculations [20–22]. Furthermore, surface irregularities and non-condensable gases may play a lesser role; a surface irregularity is not necessary to generate a bubble embryo when a high superheat is reached. Under this regime, the nucleation mechanism assumes the formation of an embryo as a spherical cap on the surface [19]. This nucleation geometry lowers the projected nucleation temperature. Experimental techniques developed to measure the superheating include monitoring the change resistance of the film heater and optical visualization of the nucleation. Optical bubble visualization also allows tracking the bubble morphology dynamics. Specific nucleation sites are reported, at high superheats, followed by the formation of a vapor film spreading on the heater area and later vertical expansion. Preferred nucleation sites are highly repeatable at short or high heating times [23]. Localized nucleation sites at homogeneous boiling may be a result of attractive forces between the fluid molecules and the solid in contact with it. Fluid molecules near the solid surface may experience large attractive forces thus increasing the nucleation temperature above the spinodal limit. Using the molecular attractive forces reasoning, numerical modeling has shown homogeneous boiling can occur in the fluid filling a cavity of the order of nanometers [24].

High fluid superheat results in high internal bubble pressures at nucleation. The growth, maximum size and collapse of a microbubble produces an unusual microbubble pressure signature during the early expansion phases. Of the limited pressure work, Zhao et al. [11] and Glod et al. [25] measured acoustic pressure fluctuations at a small distance away from a heater in a semi-infinite unbounded fluid environment. The internal bubble pressure and growth rate were back calculated based on a spherical bubble assumption and the measured acoustic pressure. The presence of two maximums in the bubble pressure signature result from the initial bubble expansion and from the bubble regrowth. Bubble regrowth occurs after the bubble collapse at the end of the first bubble growth and collapse phase. The regrowth could be due to compression and later expansion of noncondensable gas within the bubble during the bubble collapse [26]. Despite the previous experiments, more work is needed to expand the understanding of microbubble growth in confined geometries and its impact on the pressure generation.

This paper contributes to the characterization of the bubble lifecycle for water in a bounded microheater under different energy and power conditions. The characterization is carried out from optical measurements of the bubble size and bubble growth rate, and from concurrent measurements of the heater temperature during heating pulses. Mechanical bubble efficiency is determined assuming a bubble hemispherical cap shape.

2. Experimental equipment and procedure

The microheaters in this study are representative of typical TIJ devices with the nozzle plate removed and including a thin passivation layer separating the heater from the fluid, barriers surrounding the heater area, and channels to supply the fluid. The passivation layer isolates the microheater electrically from the fluid and provides a mechanical protection against the concentrated pressure during the bubble collapse. The microheater of 41 × 45 μm is centered under a fluid volume that is formed by vertical walls of 25.4 μm high and two microchannels on each side to supply fluid. The sidewalls affect the heat transfer and the pressure field generated by confining the bubble expansion process.

The TIJ device is encapsulated in two plexiglass plates. Deionized water is supplied through lateral ports on the plexiglass plates. The micro-heater operates continuously at specific frequencies in a mode where the bubbles grow and collapse without detachment from the heated surface. The growth phases of the bubbles are imaged through a short strobe light of 120 ns synchronized with the heating pulse and recorded with a microscope and digital camera. Fig. 1 shows a schematic of the experimental equipment. The strobe light time delays are varied to reconstruct an ensemble of the boiling event statistically.

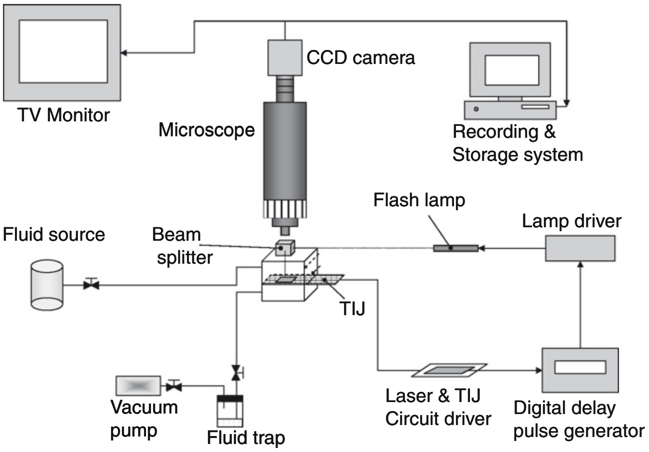

Fig. 1. Experimental set up.

The heater input power is controlled by changing the voltage from 8 to 12 V and the heating time is varied from 2.3 to 5.3 μs to change the total input energy. Experiments are performed at ambient pressure and room temperature (101.3 kPa, 296 K). Several experiments under the same driving conditions were repeated on different heaters to validate consistency.

The circuit (Fig. 1) driving the microheater uses a microprocessor, Ubicom SX28AC/DP, programmed to trigger the microbubble and the xenon flash lamp (Nanolite FX Xenon Flashlamp, High-Speed Photo-Systeme). The microprocessor activates a Darlington array that feeds a regulated voltage (8–12 V) to an individual microheater. The circuit is powered by a laboratory power supply (72–280 TENMA). The flash lamp is synchronized to the heating pulse at different time delays through the digital delay/pulse generator (DG-535, SRS), and the boiling events are captured with a microscope with two optical doublers (Infinivar continuously focusable, Infinity Photo-Optical Co) and a CCD camera (TM-7200, Pulnix). The flash lamp has a nominal flash duration of 120 ns based on the half-width of the light intensity to illuminate the bubble and capture the event. The overall optical magnification factor is 32 and the heater occupies 1/9th of the field of view. The lamp illumination is aligned with the microscope using a 45° beam splitter and the images record the backscattering off the surface. Video images are recorded to a computer through a PCI video frame grabber card (Videoh! PCI, Adaptec). The microboiling events were simultaneously observed on a monitor (13” PVM-1354Q, Sony).

Image processing is carried out to determine the bubble size. Images are recorded in an MPEG3 format during experiments and individual JPEG stills are decompiled. The still images are processed by subtracting a background mask frame, filtering out high frequency noise, passing the output through a threshold, and overlaying spatial masks (Table 1). The effectiveness of the image processing was determined by manually identifying the bubble area for a small subset of the data. The manually observed bubble area was compared to the image processing result and the error was estimated. The image processing method under-predicts the area by a factor of 1% for small bubble areas and 8% when bubble reaches its maximum size. Detailed steps of the image processing technique are given in Escobar-Vargas et al. [27].

The temperature of the microheaters was measured from changes of electrical resistance measured with a Wheatstone bridge and a differential amplifier. This technique has been used previously by other researchers [9,19]. The Wheatstone bridge voltage difference was converted to the corresponding heater change of electrical resistance [28]. This heater resistance was later converted to temperature measurements.

Fig. 2 shows the Wheatstone bridge configuration used for temperature measurements. Balancing of the Wheatstone bridge was achieved by measuring the resistance of the elements and adding small resistor values to R_3 in the bridge. The zero output voltage at the differential amplifier was checked at low input voltages $e_i = 1$ V. During experiments at high voltage, some inductance peaks at the start and end of the heating were reduced with inductor and capacitor elements.

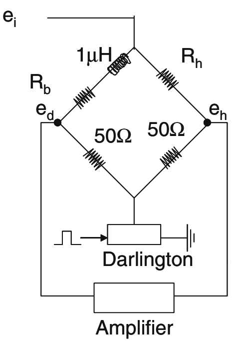

Fig. 2. Wheatstone bridge configuration, the microheater is represented by R_h.

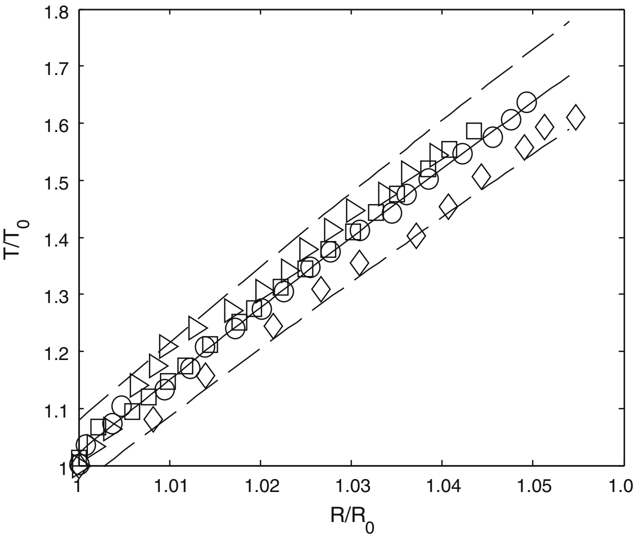

Fig. 3. Temperature calibration for a microheater.

Temperature calibrations for the microheater were obtained by introducing a TIJ array into an oven (Barnstead/Thermolyne model F48015). Small voltages of 0.1 V were applied to a microheater both as constant voltages and in a square waveform to verify the transient response. The microheater response was captured on an oscilloscope (54624A, Agilent, with a sampling rate of 200×10^6 Samples/s and peak detection of 5 ns). The oven was set to a fixed temperature and allowed to stabilize for 1 min after which the microheater resistance was recorded. This process was repeated for different temperatures in a range from 296 to 483 K. No evidence of hysteresis was found after the microheater was cooled to a previous measured temperature. Fig. 3 shows the results of the calibration for four different microheaters. Tests were carried out and the data is represented by a fit line (continuous solid line in Fig. 3). The maximum variation from tests to the fit line is calculated and represented by the dashed lines in Fig. 3. The band of data variation corresponds to ±5.6% the predicted value by the fit

Table 1
Bubble image processing.

Processing step	Operation	Purpose
1	Image registration	aligns image with background frame to remove small spatial shifts due to vibration of the apparatus
2	Background subtraction	subtracts a non bubble image to remove shadows and TIJ features
3	Image normalization and smoothing	rescales difference based on local image intensity, amplifies shadowed regions
4	Thresholding	identifies bubble regions by minimum threshold
5	Morphological closing and opening	removes holes in the bubble image (closing), and restores the external shape (opening)

approximation. The temperature range of the calibration was limited by the TIJ device thermal resistance. The TIJ device started to fail at locations different than the micro heater, e.g. electric traces and pad contacts, when it was subjected to higher temperatures. Since the tests showed a near linear trend in the temperature and in the absence of higher temperature calibration data, the curve fit is extrapolated for the experimental data.

3. Results

The projected bubble area was measured for a set of four different heating times of 2.3, 3.3, 4.3, and 5.3 μs. For each case, the bubble lifecycle was recorded from nucleation until collapse. Typically, the bounded bubble lifecycle lasts up to 14 μs. Temperature measurements were recorded only during the heating time. The water measured nucleation temperature ranged from 588 to 594 K for 3.1 W heating power.

3.1. Bubble Measurement

The microbubble life cycle is composed of nucleation, growth, maximum size, collapse and regrowth. Fig. 4 shows typical stills for different bubbles at different points in the bubble lifecycle as viewed from above. The bubble contour blurring effect results from fixing the focus plane on the substrate and the continuous change of the bubble height. The first image shows the heater with shadows generated from surface features on the device. The heater is at the center of the image, two channels and two side walls (barriers) enclose the heater. The early stage of bubble growth frames show bubbles nucleating near the center of the heater (Fig. 4b). Following nucleation, the bubble film growth phase is dominated by a very rapid expansion over the heater surface shown in frames 4c and 4d. With continued expansion, the bubble develops into a nearly hemispherical shape. The higher contrast in frames 4e and 4f indicates that the upper surface is curved and smooth. In frame 4e the bubble has expanded beyond the limits of the barriers and into the channels that supply fluid. Frames 4f, 4g, and 4h show different steps in the collapse process. Rigid surfaces affect the geometry and pressure of the collapsing bubble [29] as shown by the preferential direction for bubble collapse. The effect of the geometry in the collapsing is noticed in frame 4g where the bubble shows a more rapid collapse at the locations of the channels.

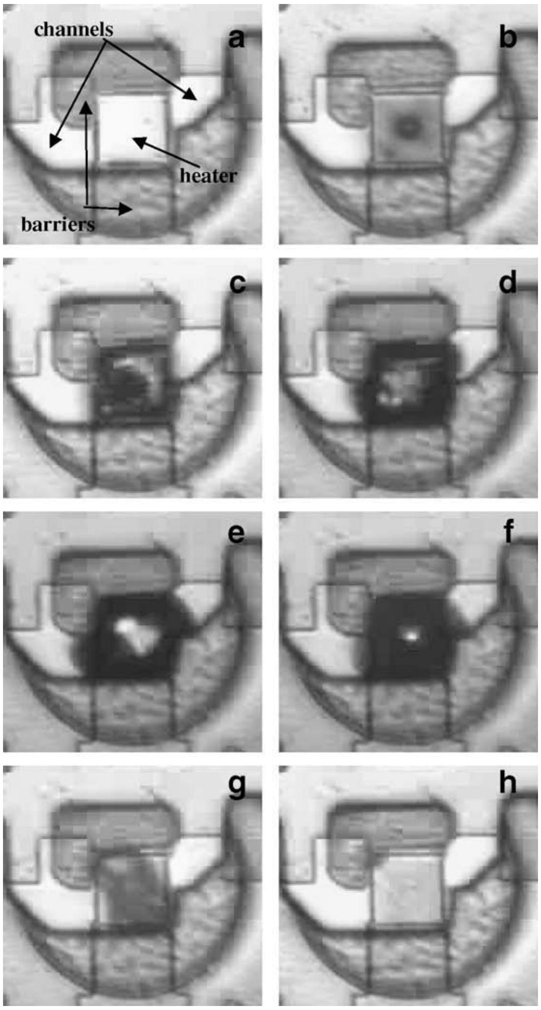

Fig. 4. Bubble life-cycle (a) heater prior to heating, (b) bubble time, 2.4 μs, (c) bubble reaches boundary constraint, 3.2 μs, (d) vertical bubble expansion, 3.9 μs, (e) maximum bubble size, 6.2 μs, (f) bubble collapsing phase, 8.2 μs, (g) 10.2 μs and (h) 12.2 μs.

Multiple bubble images are obtained and the bubble size measured to determine the mean bubble projected area. Fig. 5 shows the frequency distribution for a heating time of 4.3 μs; the total points legend indicating the number of bubble frames used to measure bubble areas. These figures show the bubble distribution at different phases, 5a during initial growth, 5b during the intermediate growth, and 5f during collapse. All figures show an approximate normal distribution. The statistical distribution is similar to a normal distribution but skewed to the right for the growing bubble phase (Fig. 5c) and initial collapse (Fig. 5d), and slightly skewed to the left for reducing bubble size (Fig. 5e). The skewness of the distribution is driven by the bubble reaching the heater area and being bounded by the side barriers. The evolution by phases of the bubble area formed by a heater with a 3.11 W and 13.4 μJ input conditions is shown in Fig. 6. A local bubble maximum is present between phases I and II and a global maximum is present between phases III and IV. The bars in Fig. 6 indicate 1.96 times the standard deviation of the experimental realizations centered about the mean, indicating the bound for the cycle to cycle variation in bubble size. Fig. 6 uncertainties can be the result of variations in the nucleation time. Nucleation time variations would result by the presence of gas molecules in the liquid, where gas molecules may act as nucleation sites promoting the formation of bubbles.

Fractional uncertainties on the measuring technique were estimated on the different variables. The fractional uncertainty in the voltage is ±0.0066, the heater resistance fractional uncertainty is $\pm 6.01 \times 10^{-4}$, the propagated fractional uncertainty on the input power is ±0.0133. The fractional uncertainty on the heating time is ±0.0087 and the propagated fractional uncertainty on the input energy to the heater results in ±0.0159. The maximum fractional uncertainty on the strobe light activation is ±0.03. The bubble area is measured by counting the bubble total number of pixels multiplied by the heater pixels scale conversion factor. The uncertainty on the number of pixels was measured manually from a set of bubble images resulting in maximum fractional uncertainty ±0.08. The scaling factor uncertainty was computed from the optical magnification and resolution resulting in ±0.085 therefore the propagated fractional uncertainty on determining the bubble area is ±0.116.

Fig. 7 shows the measured bubble area for different heating durations and approximately the same heating rate (variation in total input energy). The zero time value corresponds to the initiation of heating. For a short heating time of 2.3 μs and an input power to the heater of 3.11 W; the energy to the heater is 7.2 μJ. This amount of energy results in an incipient nucleation time of 2.5 μs and at full growth the bubble fills the volume enclosed by the heater and the walls. The maximum size is reached after the

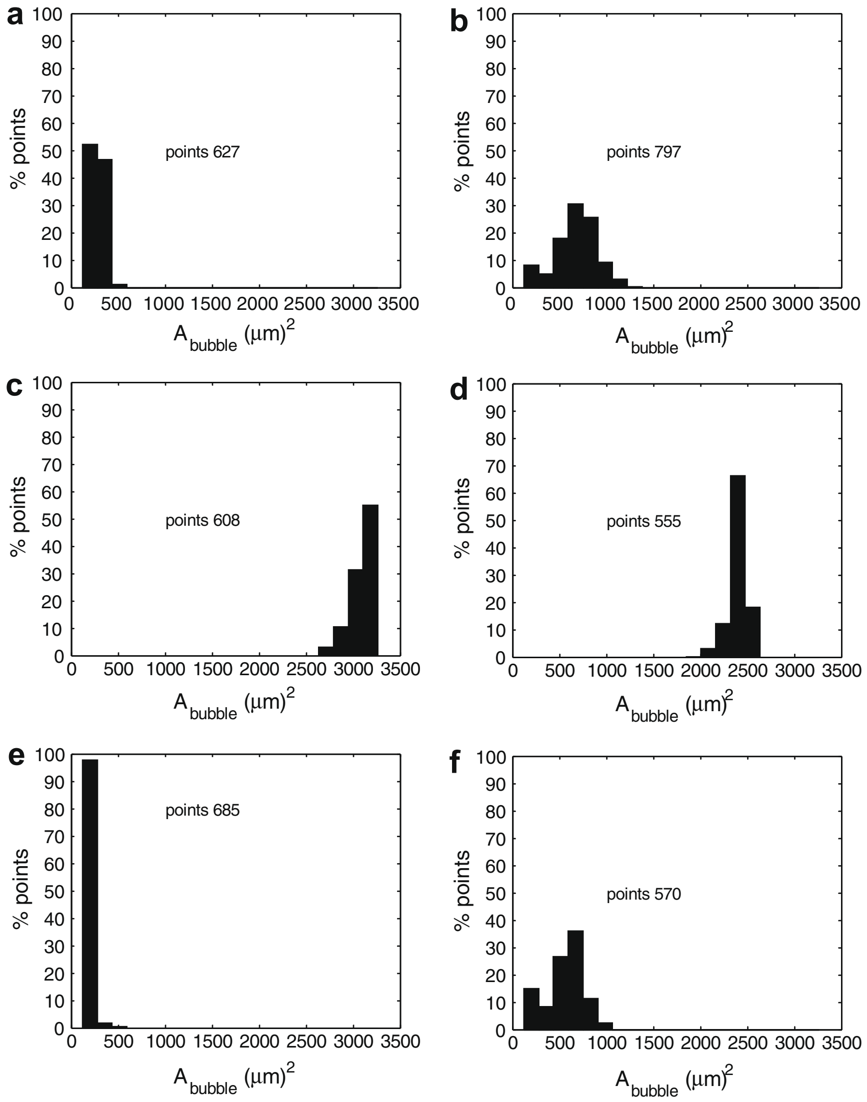

Fig. 5. Data distribution for heating time at 4.3 μs, energy 13.4 μJ and power 3.11 W. (a) 2.6 μs (b) 3.2 μs (c) 7.0 μs (d) 10.0 μs (e) 13.0 μs (f) 15.0 μs. Microheater dimensions are 41 × 45 μm.

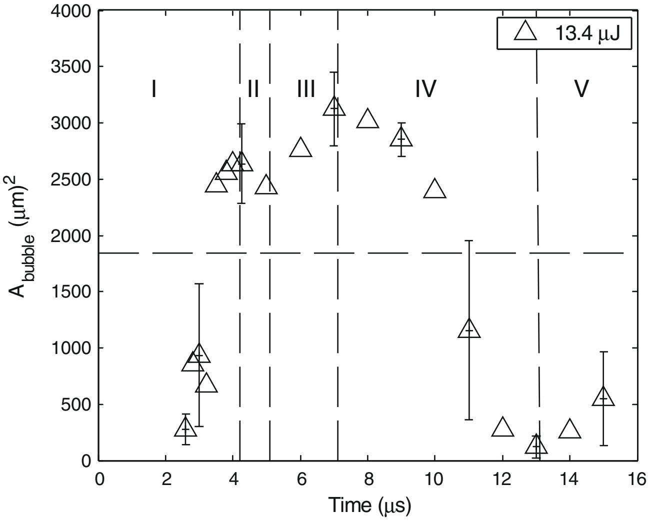

Fig. 6. Bubble area development. Bars indicate bounds for 95% data confidence. Horizontal dashed line indicates heater area 1845 μm^2.

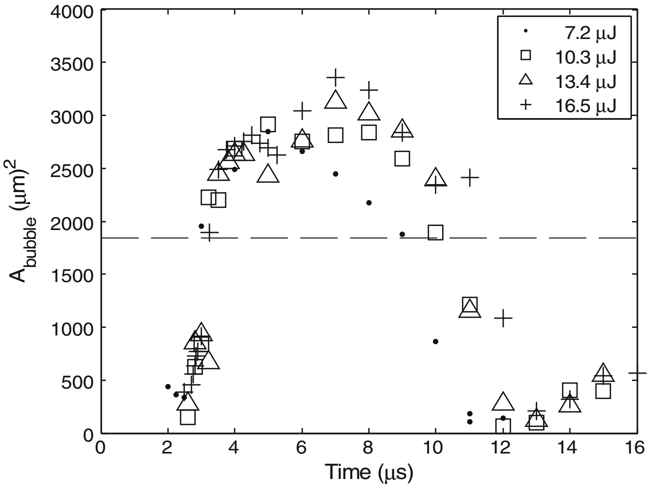

Fig. 7. Variation in total input energy, constant heating rate (applied power of 3.11 W). Dashed line indicates heater area 1845 μm^2.

end of heating duration. A bubble collapse phase occurs over a longer time compared to the growth phase.

A heating time of 3.3 μs and input power of 3.11 W (input energy of 10.3 μJ) is also shown in Fig. 7. This case results in a local maximum in the measured bubble projected area at approximately 5 μs followed by a shrinking in the bubble area and by later bubble area regrowth. The first local bubble area maximum corresponds to the instant the bubble has covered the area of the microheater and penetrated partially into the two channels adjacent to the heater. The dip in area, around 5 μs, becomes more prominent as the input energy is increased (Fig. 7 cases at 13.4 and 16.5 W). Maximum bubble area and longevity of the bubble are associated with the input energy.

Similar behavior of initial bubble growth–shrink–growth in quasi steady and pulse heating have been reported for heterogeneous boiling [30]. The transient bubble shrinking in heterogeneous boiling is explained as the result of water subcooling and bubble pressure variation. Researchers have found the bubble shrinking caused by the subcooling effect is also present in homogeneous boiling [31]. Additional research on microbubble dynamics [32] report changes in the slope of the bubble growth rate with no shrinkage in size before the maximum bubble size. These other works claim the bubble dynamics is related to its kinetic energy and reflected in the advancing contact angle [32]. Changes in contact angle may introduce different surface curvatures that along with surface tension may result in forces that change the bubble growing slope. In all these cases the bubble growth rate is relatively slow.

In the present work, the shrinking is present in the timescale range of 4–5 μs after initiation of heating. Heating cases of 4.3 μs presented the shrinking near the end of the heating; however, heating cases of 5.3 μs present the shrinking before reaching 5 μs. Fig. 7 indicates there is an energy threshold over which bubble shrinking occurs. Above the energy threshold, the bubble shrinking is always present in the range of 4–5 μs. The reduction in the bubble area may be a result of the subcooling, local variation of the pressure field, and surface tension driven change in curvature of the bubble. Numerical computations indicate the fluid near the heater (under 0.7 μm at 5 μs) is superheated, therefore, the lateral film expansion is the propagation of a nucleation front into the superheated layer. Later bubble expansion is complicated resulting from heat transfer after it reached the limit of the superheated liquid region and the dynamic variation in local pressure field. The surface tension is also important, from the moment the bubble starts growing until the interfacial acceleration reaches a maximum [33]; however, in this work the surface tension and the bubble curvature change, during the transition from inertia to heat transfer dominated growth, may contribute to the bubble shrinking. Axissymmetic contributions of the curvature contribute to the pressure field via the Rayleigh–Plesset equation (Eq. (1)). Irregular bubble shapes have different radius of curvature at the interface. Therefore the bubble interface is subjected to nonuniform force magnitudes due to the different radius of curvature as seen from Eq. (1).

$$p_v - p_o = \rho_l r \frac{d^2 r}{dt^2} + \frac{3}{2}\rho_l \left(\frac{dr}{dt}\right)^2 + \frac{4\mu_l}{r}\frac{dr}{dt} + \frac{2\sigma}{r} \tag{1}$$

where p_v is the internal bubble pressure, p_o the ambient pressure, ρ_l the liquid density, r the bubble radius, μ_l the liquid viscosity, and σ the surface tension.

After the bubble reaches the global maximum size and collapses completely, a second regrowth of small bubbles occurs. This phenomenon was observed and reported by other researchers inferring that it could be due to compression of noncondensable gas within the bubble during the bubble collapse [26]. The presence of nanobubbles after bubble collapse during two consecutive heating pulses has been demonstrated [34]; nanobubbles may grow slightly dissipating accumulated energy from the residual superheat. The present results are consistent with the residual superheat combined with nanobubbles or non-condensible gases. In addition, the reflection of local high pressure waves [35] may be a key factor in the final bubble regrowth.

Fig. 8 reflects the effect of the heating rate on the nucleation time, maximum bubble size, and the bubble growth. Increasing input power (heating rate) in the bubble generation results in a larger bubble growth rate; also, higher input power causes the nucleation time shift to earlier times [11,19,21,27]. The nucleation times and maximum bubble size are associated to the power density.

3.2. Growth rate

Experimental data was collected at nonuniform time intervals. Therefore, the bubble radius growth rate is calculated from a local linear average approximation to three points.

Fig. 9a depicts the effect of the applied power. The net result is as expected, larger radial velocity results due to a larger power input. The maximum speed and bubble acceleration changed with power as well. The bubble growth is independent of the applied energy as seen in Fig. 9b. After the bubble reached the maximum size, the collapse phase is the same for all the measured cases. Energy was applied for short periods of time (maximum 5.3 μs) and the bubble collapse occurred some time after the energy was cut. The collapsing velocity was nearly constant during the experiments as seen in Fig. 9b.

During heating and prior to bubble nucleation the fluid layers closest to the solid heater are superheated. When nucleation occurs the bubble is highly superheated and the growth is inertia dominated during the early times [13]. Previous experimental works computing the bubble growth assume a spherical bubble growth and calculate the internal bubble pressure for later bubble growth analysis. The spherical assumption is valid just after the time of incipient nucleation and unbounded fluids in homogeneous boiling. Microbubble shapes in bounded fluids can differ significantly from spheres and a different approach is used in this case. Experimental data from this work was analyzed during the bubble growth. Two slopes are noticed, the first slope corresponds to the bubble film growth rate (Fig. 6 region I) and the second slope is determined from the times near the maximum bubble (Fig. 6 region III) and is considered to indicate the bubble volumetric

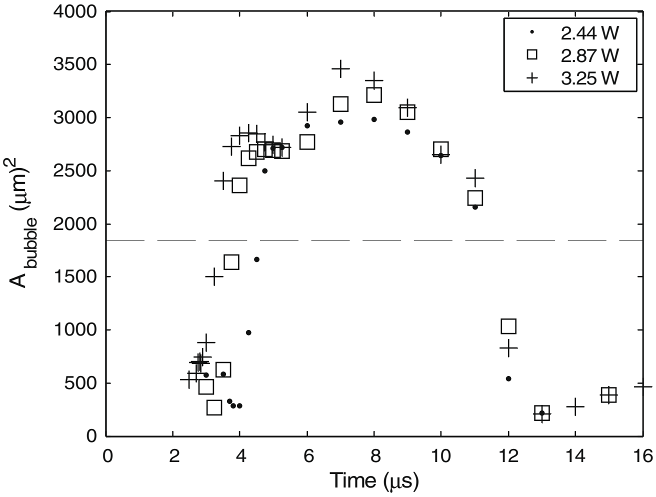

Fig. 8. Bubble lifecycle for different power. Dashed line indicates heater area 1845 μm^2.

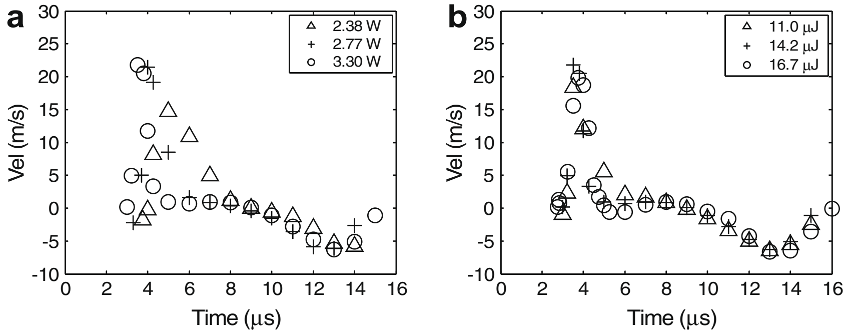

Fig. 9. Bubble growth rate. (a) Effect of heating power; (b) effect of energy (constant power 3.3 W).

growth rate. In an effort to assume a shape that has a close representation of the bubble, the bubble is assumed to have different shapes during its growth. During phases I and II (Fig. 6) the bubble is assumed to have a spherical cap shape. The spheric cap dimensions are given by r_1 and h (Fig. 10) where r_1 h. r_1 is defined as a “film radius” and h is defined as height. During phase III the bubble is assumed to have a hemispherical shape $r_1 = h$. The hemispherical cap bubble shape assumption is made based on the bubble evolution observed from the stills (e.g. Fig. 4c) where the formation of a vapor film is observed. The hemispherical bubble shape assumption is deduced from the bubble image Fig. 4e where the bubble surface shows a pronounced curvature compared to Fig. 4c and d. The film dimension r_1 is determined from fitting lines (Fig. 11a) on the bubble data for phases I, II; $r_1 = h$ during phase III. The “volumetric dimension” h is assumed to follow a fit line (Fig. 11b) passing through the bubble incipience time and the points at phase III. The volumetric growth h was calculated using two different approaches selected from the bubble growth mode; a linear fit that may indicate inertia dominated growth and a square root fit that may depict a heat transfer dominated growth as shown in Fig. 11.

The radius of curvature of the hemispherical cap is estimated to determine the internal bubble pressure. Eq. (2) gives the relationship between the radius of curvature and the characteristic lengths of the hemispherical cap,

$$r = \frac{r_1^2 + h^2}{2h}, \tag{2}$$

where the radius of curvature r of the hemispherical cap is used to calculate the change of pressure in the Rayleigh–Plesset equation (Eq. (1)).

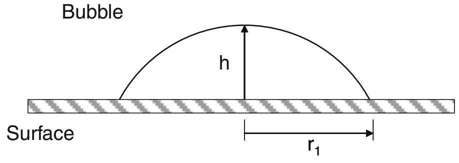

Fig. 10. Hemispherical cap bubble and its characteristic distances.

The bubble mechanical energy is defined as the work done by the bubble expansion, due to its high internal pressure. The bubble expansion has to use some energy to expand versus the ambient pressure and versus the fluid surface tension. Therefore, the extractable mechanical energy is defined as the work done by the bubble internal pressure minus the work done on the bubble by the atmospheric pressure and the work done on the bubble due to the surface tension. Changes in pressure relate the extractable mechanical energy by the bubble change of volume. The extractable mechanical energy is defined by Eq. (3) [25]

$$E_m = \int \left(p_v - p_o - \sigma \frac{dA}{dV} \right) \frac{dV}{dt}\, dt, \tag{3}$$

where A and V are the liquid–vapor surface area and volume of the hemispherical cap, respectively. In terms of the cap volume and characteristic lengths the extractable mechanical energy is given by Eq. (4)

$$E_m = \int \left(p_v - p_o - \frac{2\sigma}{h} \right) \frac{dV}{dt}\, dt, \tag{4}$$

The extractable power results from the derivative of Eq. (4). The mechanical efficiency is calculated for the data using Eq. (5)

$$\eta = \frac{E_m}{E_{in}}, \tag{5}$$

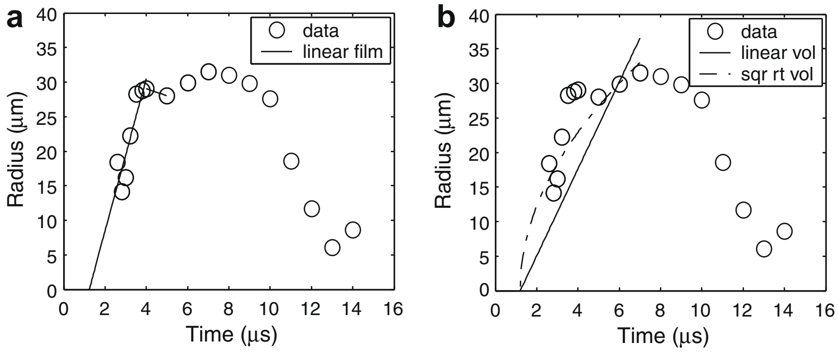

Fig. 11. Bubble growth regime fitting lines on experimental bubble radius data: (a) Film growth and receding, linear sections. (b) Volumetric growth, square root, linear. Input conditions: power 3.05 W, heating 5.3 μs.

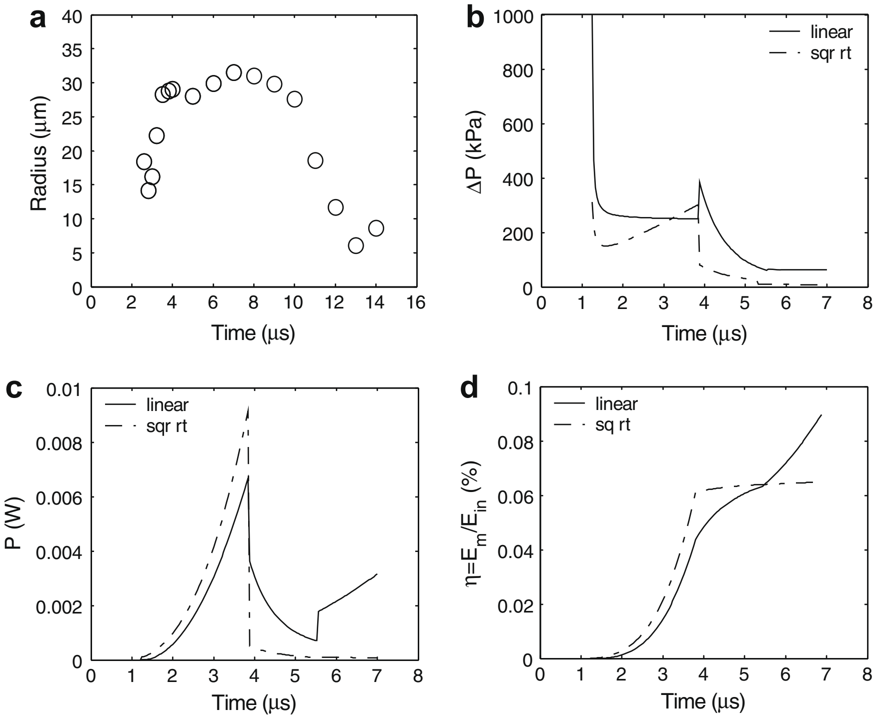

Fig. 12. Data analysis. (a) Bubble radius lifecycle; (b) pressure difference $p_v - p_o$; (c) Power derived from the extractable mechanical work and (d) Efficiency.

where E_m is the extractable mechanical energy from the bubble and E_{in} is the input energy to the microheater.

The experimental data, pressure difference, mechanical power derived from the bubble, and efficiency are shown in Fig. 12. Based on curve-fit relationships for the different growth phases; the general behavior of the variation in pressure can be estimated. Jumps in the pressure are artifacts of the transition from one fit to another which are limited by the resolution available in the experiment. Useful extractable mechanical work is developed only during the bubble expansion; therefore, the computations stop at the maximum bubble size. The bubble mechanical efficiencies are calculated using linear and square root approaches for the volumetric growth (Fig. 13). Maximum observed mechanical efficiencies do not exceed 0.32%. Fig. 13 does not show an asymptotic trend, and since the bubble expansion velocity (dr/dt) increases with the input power, it is reasonable to assume that there is possible room to improve the mechanism and increase the mechanical efficiency of the bubble. Increasing the bubble growth rate requires an increase in the input power. However, efficiency does not necessarily increases with input power (Fig. 13). Input energy is distributed to increase the internal energy of the heater film and the fluid; energy is also consumed during the phase change process [36]. The energy fraction used for the change of phase affects directly the extractable mechanical work. Larger values of heating rate and less energy need to be explored to find the maximum achievable mechanical efficiency.

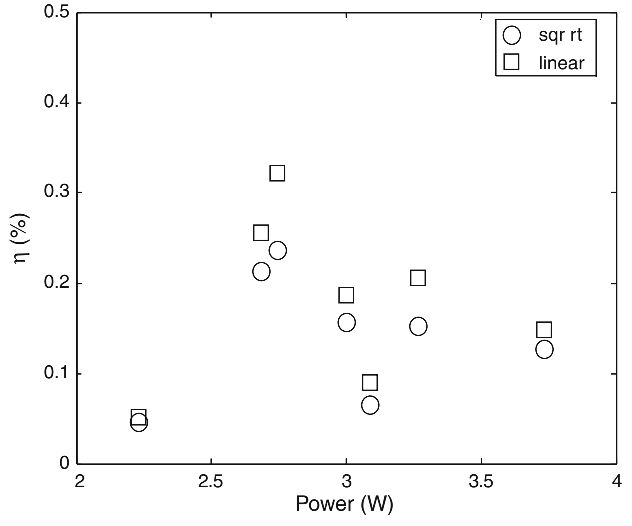

Fig. 13. Bubble maximum efficiency for different input power.

3.3. Temperature measurement

The heater electrical resistance was measured and the temperature calculated from the calibration curve (Fig. 3) by assuming uniform temperature on the microheater. Previous work has shown an inflection point on temperature measurements as an indication of the incipient nucleation [9,10,19]. The incipient nucleation time, from measurements of change resistance on gold microheaters and from bubble visual inspections, was reported to shift up to 0.2 μs [10]. Experimental studies of temperature using heater configurations without a passivation layer show a clear inflection point at nucleation for some microheaters [9,19]. In this study, an inflection point in the temperature was not observed due to the passivation layer. The temperature was measured synchronized with the visualization. The nucleation time was determined by extrapolating the bubble area measurement back in time to the point of zero initial area. The nucleation temperature is then determined at the specific nucleation time and fluid temperature is estimated based on the temperature drop through the passivation layer.

Fig. 14 shows temperature measurements for the four different heating times, the zero value in the time axis represents the initi-

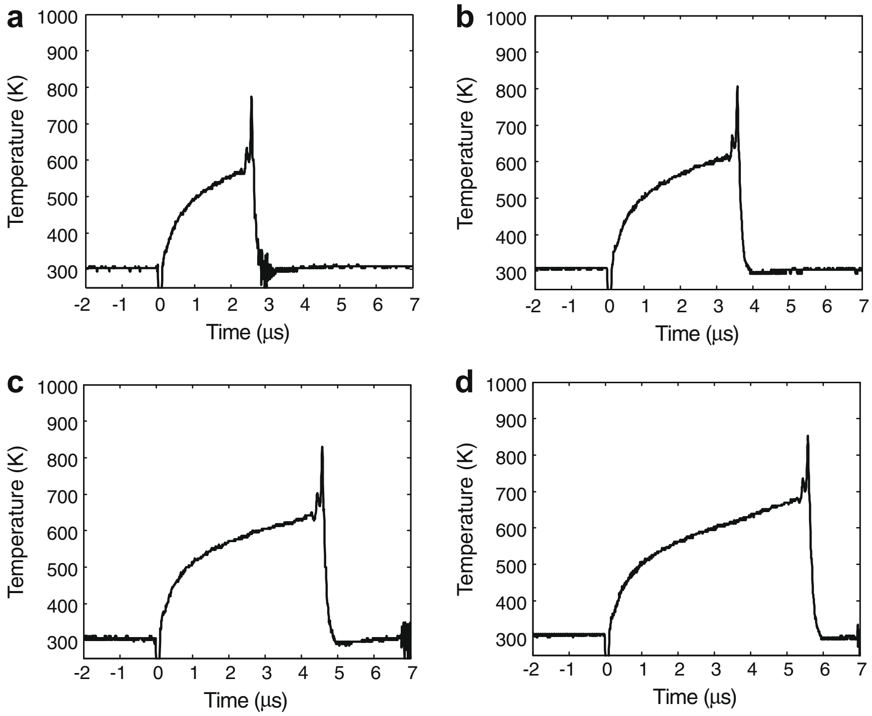

Fig. 14. Heater temperature for power of 3.11 W and (a) heating 2.3 μs, energy 7.2 μJ; (b) heating 3.3 μs, energy 10.3 μJ; (c) heating 4.3 μs, energy 13.4 μJ and (d) heating 5.3 μs, energy 16.5 μJ.

ation of the heating. Temperature nucleation fractional uncertainties for the same input power resulted in 0.01. For all cases, the heating rate rises rapidly up to 3.7×10^7 K/s. The corresponding measured incipient nucleation times and heater temperatures for the studied cases are: 2.8 μs; 2.65 μs ($T = 588$ K); 2.7 μs ($T = 594$ K); and 2.7 μs ($T = 589$ K), respectively. The effect of the total energy released can be observed from the maximum temperature reached at the end of the heating time. The spike in the curve at the end of the heating is not physical but due to inductance in the circuit when the voltage is dropped.

Table 2 lists the resulting incipient nucleation time and temperature for different input voltages, powers, and energies. Large input powers result in larger heating rates with the nucleation occurrence at earlier times. The nucleation temperatures are close to the superheat limit and they are indicative of the homogeneous boiling mode. Superheat limit theory establishes an approximate maximum incipient nucleation temperature for water of 556 K based on the Kwak and Panton thermodynamic model [19,37]. Other work has measured the superheat temperature limit of 575 K [25] and calculated 577 K [13]. In the present experiments, the passivation layer produces a larger heater temperature at the onset of nucleate boiling due to an increased thermal resistance between the heater and fluid. The magnitude of this effect has been estimated through a 1-D unsteady simulation of the heat conduction up to the incipient nucleation and indicates a 12–15 K difference between the heater and fluid temperature. The 15 degree difference results in a fluid mean nucleation temperature of 575 K. Different heating techniques have been used to measure the limit of superheat for water resulting in temperatures of 575.2 K when pulse heating is used; 553 K when bubble column by isobaric droplet heating is used [38].

Table 2
Boiling conditions for 5.3 μs time heating.

Voltage (V)	Power (W)	Energy (μJ)	$t_{\mathrm{nucleation}}$ (μs)	$T_{\mathrm{nucleation}}$ (K)
10.5	3.25	17.2	2.70	574
9.87	2.87	15.2	3.03	547
9.11	2.44	12.9	3.72	516

3.4. Discussion

Fig. 8 shows that for given experimental conditions, the nucleation times were on the order of 2.6–3.7 μs. The nucleation temperature is near the superheat limit and compares to other results reported in literature (Table 3). Both the early nucleation time and the high superheat are consistent with a homogenous boiling mode or heterogeneous nucleation on a smooth non-wetting surface [19], but not of cavity induced heterogeneous nucleation.

The fast bubble expansion as consequence of the high heat rates is manifested in Fig. 9. The immediate transition of the bubble nuclei into a vapor film results in a fast inertia dominated lateral expansion due to the large energy distributed on the heater area and a short temperature penetration depth into the fluid at the initial times. The bubble growth shows a shrinking of the observed bubble area around 4–5 μs for large input energy cases. This dwell is clear in Fig. 7 for heating times of 4.3 and 5.3 μs (13.4 and 16.5 μJ, respectively). The heater fluid subcooling, local pressure

Table 3
Reported homogeneous temperatures by other researchers.

$T_{\mathrm{nucleation}}$ (K)	Heating rate (K/s)	Reference
573	4.2×10^7	Thomas et al. [9]
556	2.5×10^8	Avedisian et al. [19]
576	8.6×10^7	Glod et al. [25]
568	9.3×10^7	Iida et al. [41]
563	9.0×10^7	Derewnicki [42]
575.2		Avedisian [38]
575 ± 5.8	3.7×10^7	Present study

variations, and surface tension along with the bubble curvature play an important role in this feature of the bubble growth. The bubble expansion after the dwelling is dominated by the volumetric expansion and the area, as viewed in the experiment, expands at a slower rate.

The growth–shrinking–growth at 4–5 μs and the regrowth at the end of the bubble lifetime may affect the quality of the bubble generation and the practical functionality of devices. The bubble growth–shrinking–growth will affect the bubble expansion by introducing disturbances in the droplet generation; that may result in early droplet breakup or satellite droplets in thermal atomizers. Satellite droplets reduce the quality of spray and are closely related to the microheater chamber and the bubble formation [39]. Johnson [40] claims the energy input parameters influence the TIJ droplet generation process. Low activation energies result in a clear dwell on the droplet velocity.

The bubble film and volumetric growth are derived on the assumption of a hemispherical cap bubble growth. Computed efficiencies based on the hemispherical cap assumption resulted in small values suggesting most of the energy applied to the heater is distributed to increase the internal energy of the heater film and the fluid; energy is also consumed during the phase change process [36]. Only a small portion of energy is converted into extractable mechanical energy. Energy losses can include the heat dissipation to the silicon layer underneath the microheater, and lateral heat conduction. Efficiency results indicate the need to modify the heater design when mechanical work is required from the bubble. The maximum computed efficiency of 0.32% is a comparable order of magnitude to those (0.23%) reported by Zhao et al. [11] who computed it from acoustic bubble measurements and assuming a spherical bubble shape. Although both numbers are small there is an indication that the different geometry can lead to an relative improvement in efficiency. As this stage the mechanical efficiency of the bubble growth process is larger than the overall efficiency of TIJ droplet process. Droplets from thermal atomizers have a typical 53 μm diameter and 8.8 m/s velocity under activation energy of 4.8 μJ, the resulting efficiency calculated as the ratio of the droplet kinetic energy to the activation energy is 0.066%, hence substantial viscous dissipation of the mechanical energy is present during the drop formation process. The microheaters used in this research are similar to microheaters in regular TIJ atomizer, however, regular TIJ atomizers have a nozzle plate through which the fluid is ejected. Differences in the calculated efficiency indicate considerable energy losses from the bubble generation to the droplet ejection due to frictional losses.

4. Conclusions

This work presents the results in the characterization of the laterally bounded bubble dynamics under controlled heater input conditions. Bubble area was measured directly from images and simultaneously with the microheater temperature. A stroboscopic imaging technique was used to measure bubble area from above. Microheater temperature was acquired based on the change of electrical resistance of the microheater. The bubble mechanical efficiency was determined based on experimental data and complemented with a hemispherical cap bubble shape assumption.

It was determined that for heating times from 2.3 to 5.3 μs with input power from 2.4 to 3.25 W, very high superheats were achieved with rapid bubble growth. The input energy and heating rate resulted in characteristic nucleation time, growth rate, bubble shape, and bubble lifetime. High heating rates produce an early nucleation and fast expansion; on the other hand, the total energy input has a strong effect on the maximum bubble size and duration. The short time to nucleation and the high measured superheat indicate a homogeneous type of nucleation. These results are consistent with previous work [19,25].

The bubble growth was characterized by a rapid vapor film expansion, and later volumetric expansion. Temporary bubble shrinking was noticed at 4–5 μs for high heating rates and input energies. Bubble growth–shrink–growth is present only after a minimum energy is supplied; bubbles provided with less energy do not show a shrinking phase during the growth. The shrinking occurred independently of the heating time and it may be due primarily to bubble reaching the end of the superheated liquid region, local variation of the pressure field surrounding the bubble, and the surface tension driven change in shape of the bubble. This is the first time the behavior has been seen in these fast growth and high superheat processes.

The bubble energy conversion efficiency, calculated using bubble images and a hemispherical bubble assumption, shows a maximum inside the investigated input power range 2.4–3.7 W. The bubble efficiency is directly related to bubble size and the growth rate. Increasing the efficiency might require to explore a broader range of heating. Different geometric configurations surrounding the microheater may be explored to minimize energy losses and improve the energy conversion efficiency.

From a practical standpoint, understanding the bubble dynamics is important in TIJs reliability. The bubble dynamics characterization provides information to avoid operational conditions that may result in firing chamber starvation in TIJs due to over-energy conditions. As the bubble over-expands into the microchannels, it takes more time for the capillary filling process to replenish the firing chamber. If the microheater is activated with a dry chamber, permanent damage can occur. Bubble regrowth at the end of the bubble life time may result in undesired problems in TIJs and MEMs e.g. premature droplet ejection or fluid disturbances. Mechanical efficiency results are an indication of the amount of heat losses and the need of improving heater design in the TIJ if larger extractable mechanical efficiencies are desired from the bubble expansion.

Acknowledgments

This work was partially sponsored by the GOALI program of the National Science Foundation (NSF), Grant No. 0131994, and by Hewlett Packard Co.

References

[1] L. Lin, Thermal challenges in MEMS applications: phase change phenomena and thermal bonding processes, Microelectr. J. 34 (2003) 179–185.
[2] H.J. Trost, S. Ayers, T. Chen, W.R. Cox, M.E. Grove, R. Hoenigman, Using drop on demand technology for manufacturing grin lenses, in: Proceedings 2001, Ann. Mtg., ASPE, Raleigh, NC, 2001, pp. 533–536.
[3] D. Cibis, K. Krüger, System analysis of a DoD print head for direct wiring of conductive circuits, Int. J. Appl. Ceram. Technol. 4 (5) (2007) 428–435.
[4] M. Englmann, A. Fekete, I. Gebefügi, P. Schmitt-Kopplin, The dosage of small volumes for chromatographic quantifications using a drop-on-demand dispenser system, Anal. Bioanal. Chem. 388 (2007) 1109–1116.
[5] W. Feng, J. Fuh, Y. Wong, Development of a drop-on-demand micro dispensing system, Mater. Sci. Forum 505-507 (2006) 25–29.
[6] V. Shah, D. Wallace, Low-cost solar cell fabrication by drop-on-demand ink-jet printing, in: Proceedings of the IMAPS 37th Annual International Symposium on Microelectronics, Long Beach, CA, 2004.
[7] P. Tarcha, D. Verlee, H. Hui, J. Setesak, B. Antohe, D. Radulescu, D. Wallace, The application of ink-jet technology for the coating and loading of drug-eluting stents, Ann. Biomed. Eng. 35 (10) (2007) 1791–1799.
[8] X. Zhao, J. Evans, M. Edirisinghe, J. Song, Ink-jet printing of ceramic pillar arrays, J. Mater. Sci. 37 (2002) 1987–1992.
[9] O.C. Thomas, R.E. Cavicchi, M.J. Tarlov, Effect of surface wettability on fast transient microboiling behavior, Langmuir 19 (2003) 6168–6177.
[10] K.M. Balss, C.T. Avedisian, R.E. Cavicchi, M.J. Tarlov, Nanosecond imaging of microboiling behavior on pulse-heated Au films modified with hydrophilic and hydrophobic self-assembled monolayers, Langmuir 21 (2005) 10459–10467.

[11] Z. Zhao, S. Glod, D. Poulikakos, Pressure and power generation during explosive vaporization on a thin-film microheater, Int. J. Heat Mass Transfer 43 (2000) 281–296.
[12] A. Asai, Bubble dynamics in boiling under high heat flux pulse heating, J. Heat Transfer 113 (1991) 973–979.
[13] V. Carey, Liquid–vapor phase-change phenomena: an introduction to the thermophysics of vaporization and condensation processes in heat transfer equipment, in: Taylor and Francis Series in chemical and mechanical engineering, 1992.
[14] Y. Hsu, On the size range of active nucleation cavities on a heating surface, J. Heat Transfer 84 (1962) 207–216.
[15] B. Mikic, W. Rhosenow, P. Griffith, On bubble growth rate, Int. J. Heat Mass Transfer 13 (1970) 657–666.
[16] Zuber, Vapor bubbles in non-uniform temperature field, Int. J. Heat Mass Transfer 2 (1961) 83.
[17] V. Skripov, P. Pavlov, Explosive boiling of liquids and fluctuations nucleus formation, High. Temp. USSR 8 (1970) 782–787.
[18] M. Blander, D. Hengsterberg, J. Katz, Bubble nucleation in n-heptane n-hexane n-pentane+hexadecane mixtures and water, J. Phys. Chem. 75 (1971) 3613–3619.
[19] C. Avedisian, W. Osborne, F. McLeod, C. Curley, Measuring bubble nucleation temperature on the surface of a rapidly heated thermal ink-jet heater immersed in a pool of water, Proc. Roy. Soc. 455 (1999) 3875–3899.
[20] L. Lin, K. Udell, A. Pisano, Liquid–vapor phase transition and bubble formation in micro structures, Therm. Sci. Eng. 2 (1994) 52–59.
[21] Z. Yin, A. Prosperetti, J. Kim, Bubble growth on an impulsively powered microheater, Int. J. Heat Mass Transfer 47 (2004) 1053–1067.
[22] L. Lin, A.P. Pisano, V.P. Carey, Thermal bubble formation on polysilicon microresistors, J. Heat Transfer 120 (1998) 735–742.
[23] C.T. Avedisian, R.E. Cavicchi, M.J. Tarlov, New technique for visualizing microboiling phenomena and its application to water pulse heated by a thin metal film, Rev. Sci. Instrum. 77 (2006). Paper No. 063706.
[24] V.P. Carey, J. Padilla, Y. Gan, Homogeneous nucleation of vapor at preferred sites during rapad transient heating of liquid in micropassages, J Heat Transfer 129 (2007) 1333–1340.
[25] S. Glod, D. Poulikakos, Z. Zhao, G. Yadigaroglu, An investigation of microscale explosive vaporization of water on an ultrathin Pt wire, Int. J. Heat Mass Transfer 45 (2002) 367–379.
[26] Y. Hong, N. Ashgriz, J. Andrews, Experimental study of bubble dynamics on a microheater induced by pulse heating, J. Heat Transfer 126 (2004) 259–271.
[27] S. Escobar-Vargas, D. Fabris, J.E. Gonzalez, R. Sharma, C. Bash, L. Ortiz, J. Cartagena, Fast transient micro-boiling characterization, in: Proceedings of the ASME Summer Heat Transfer Conference, 2005, Paper # HT2005-72348.
[28] J.P. Holman, Experimental Methods for Engineers, second ed., McGraw-Hill, New York, 2001.
[29] J.R. Blake, D.C. Gibson, Cavitation bubbles near boundaries, Ann. Rev. Fluid Mec. 19 (1987) 99–123.
[30] J. Li, G.P. Peterson, Microscale heterogeneous boiling on smooth surfaces–from bubble nucleation to bubble dynamics, Int. J. Heat Mass Transfer 48 (2005) 4316–4332.
[31] J. Xu, W. Zhang, Effect of pulse heating parameters on the microscale bubble dynamics at a microheater surface, Int. J. Heat Mass Transfer 51 (2008) 389–396.
[32] I. Yang, F. Tseng, C. Chang, C. Chieng, Microbubble formation dynamics under high heat flux on heaters with different aspect ratios, Nanoscale Microscale Thermophys. Eng. 10 (2006) 1–28.
[33] A.J. Robinson, R.L. Judd, The dynamics of spherical bubble growth, Int. J. Heat Mass Transfer 47 (2004) 5101–5113.
[34] R.E. Cavicchi, C.T. Avedisian, Bubble nucleation and growth anomaly for a hydrophilic microheater attributed to metastable nanobubbles, Phys. Rev. Lett. 98 (2007) 124501.
[35] C.E. Brennen, Cavitation and Bubble Dynamics, Oxford University Press, 1995.
[36] O.E. Ruiz, CFD model of the thermal inkjet droplet ejection process, in: Proceedings of ASME–JSME Thermal Engineering Summer Heat Transfer Conference, 2007, Paper No. HT2007-32427.
[37] H. Kwak, R. Panton, Tensile strength of simple liquids predicted by a model of molecular interactions, J. Phys. D 18 (1985) 647–659.
[38] C.T. Avedisian, The homogeneous nucleation limits of liquids, J. Phys. Chem. Ref. Data 14 (1985) 695–720.
[39] F. Tseng, C. Kim, C. Ho, A high-resolution high-frequency monolithic top-shooting microinjector free of satellite drops – Part II: Fabrication, implementation, and characterization, J. Microelectromech. Syst. 11 (2002) 437–447.
[40] D. Johnson, The effect of heating pulse shape on drop size and stability in thermal inkjet, SPIE 1670 (1992) 224–229.
[41] Y. Iida, K. Okuyama, K. Sakurai, Boiling nucleation on a very small film heater subjected to extremely rapid heating, Int. J. Heat Mass Transfer 37 (1994) 2771–2780.
[42] K. Derewnicki, Experimental studies of heat transfer and vapor formation in fast transient boiling, Int. J. Heat Mass Transfer 28 (1985) 2085–2092.